energies

MDPI

Article

Numerical Study of the Mechanisms and Co-Optimization of CO_2 Storage with Enhanced Gas Recovery in a Tight Gas Reservoir

Pengcheng Liu [1,2], Xinyu Zheng [3], Lili Liu [1,2], Jun Liu [1], Xinwei Liao [3] and Zepeng Yang [3,*]

[1] PetroChina Changqing Oilfield Company, Xi'an 710018, China
[2] National Engineering Laboratory of Low-Permeability Oil & Gas Exploration and Development, Xi'an 710018, China
[3] College of Petroleum Engineering, China University of Petroleum (Beijing), Beijing 102249, China
* Correspondence: yzp6085060@163.com

Abstract

CO_2 storage with enhanced gas recovery (CSEGR) can raise recovery in tight sandstone reservoirs while retaining injected CO_2, but the relative influence of transport and flow properties on these two targets is rarely compared within one well-group model. A multicomponent model of a seven-well group in the eastern Sulige gas field, Ordos Basin, included CO_2 dissolution, adsorption, diffusion, threshold pressure gradient and stress sensitivity, compared under identical well controls. Injection–production strategies were evaluated by single-factor analysis, a three-factor five-level L25 orthogonal design and four supplementary runs. Following 10 years of depletion, the central well was converted to CO_2 injection. At 22 years after conversion (32 years of total reservoir development), the cumulative CH_4 recovery factor reached 29.00%, exceeding that of continued depletion at the same development time by 3.12 percentage points. Raising the threshold-pressure-gradient multiplier from 0.8 to 1.2 lowered incremental recovery by 4.07 percentage points; dissolution and adsorption each changed it by less than 0.5. Stress sensitivity lowered recovery during depletion but raised it during injection, so both stages require joint assessment. Producer bottom-hole pressure had the largest effect on recovery, followed by conversion pressure. Injecting 40 t/d at conversion and producer pressures of 4 and 3 MPa balanced both targets, giving 31.86% recovery and a net CO_2 increase of 24.12 × 10^4 t.

Keywords: tight gas reservoir; CO_2 enhanced gas recovery; numerical simulation; CO_2 storage

Academic Editor: Alberto Maria Gambelli

Received: 10 October 2026
Revised: 20 November 2026
Accepted: 24 November 2026
Published: 27 November 2026

Copyright: © 2026 by the authors. Licensee MDPI, Basel, Switzerland. This article is an open access article distributed under the terms and conditions of the Creative Commons Attribution (CC BY) license.

1. Introduction

Natural gas is an important transition fuel in the shift to a low-carbon energy mix, and tight sandstone gas has become one of the main sources of reserve and production growth in China [1,2]. Tight sandstone gas reservoirs have low permeability, which limits pressure propagation and gas production during depletion and keeps both the produced fraction of well-controlled reserves and the ultimate recovery factor low. The Sulige gas field in the Ordos Basin is the largest tight sandstone gas field in China; its reservoirs are characterized by low permeability, low pressure, low abundance and strong

 https://doi.org/10.3390/en19235762

heterogeneity, and the predicted recovery factor under depletion is generally only 30–40% [3,4]. CO_2 flooding for enhanced gas recovery (CO_2-EGR) promotes CH_4 production through pressure support, displacement and compositional mass transfer, and places part of the injected CO_2 in the reservoir, which provides a way to raise gas recovery and store CO_2 at the same time [5–7]. Under the carbon peaking and carbon neutrality targets, injecting CO_2 into depleted or nearly depleted gas reservoirs serves both enhanced recovery and geological storage, and is one of the main directions of carbon capture, utilization and storage (CCUS) [7,8].

The feasibility of CO_2-EGR comes from the property contrast between CO_2 and CH_4 at reservoir conditions. At typical reservoir temperature and pressure CO_2 is supercritical, and its density and viscosity are much higher than those of CH_4, so injected CO_2 tends to advance in the lower part of the reservoir and to form a relatively stable displacement front, which delays early breakthrough [5,9,10]. CO_2 and CH_4 are fully miscible, however, and molecular diffusion together with mechanical dispersion mixes the two gases near the front. The width of the mixing zone controls the breakthrough time and the CO_2 content of the produced gas, and is therefore decisive for CO_2-EGR [11–13]. Field tests and engineering studies at K12-B in the Netherlands, Budafa in Hungary, Rio Vista in the United States and Altmark in Germany show that CO_2-EGR is technically feasible, but that breakthrough control and injectivity are common constraints [6,14–16].

Published work has examined the factors that control CO_2-EGR in tight gas reservoirs both experimentally and numerically. Jia et al. [17] discussed the roles of gas mixing, pressure maintenance and cushion-gas displacement in tight gas recovery. Zhao et al. [18–20] investigated CO_2-EGR and storage in tight gas reservoirs, with emphasis on fracture configurations, completion strategies and well patterns. Liu et al. [21] examined diffusion, adsorption and water-blocking relief through laboratory measurements and core flooding. Hu et al. [22] used experimental measurements to construct reservoir-scale models and evaluated the effects of pore-throat characteristics, reservoir heterogeneity and injection timing on gas recovery and CO_2 storage. Ding et al. [23] experimentally assessed the feasibility of supercritical CO_2 injection for simultaneous enhanced gas recovery and storage. Yan et al. [24] focused on CO_2 breakthrough and sweep efficiency in a two-dimensional fracture–matrix model and optimized fracture and injection parameters using response surface methodology. Liu et al. [25] conducted artificial-core flooding experiments to examine how depletion pressure, injection conditions and permeability affect gas recovery. Besides these transport processes, flow properties specific to tight reservoirs also affect CO_2-EGR. Dissolution of CO_2 in formation water removes CO_2 from the gas phase and alters the near-well pressure [26,27]. The adsorption capacity of rock for CO_2 is usually higher than that for CH_4, so injected CO_2 can displace part of the adsorbed CH_4 and add to CO_2 storage [7,21,28]. A threshold pressure gradient exists in low-permeability rock and leaves gas in regions of small pressure difference immobile [29–31]. Stress sensitivity reduces permeability as pore pressure declines, and laboratory observations have shown that permeability recovery during subsequent repressurization may be incomplete [32–34]. Yang et al. [35] developed a full-lifecycle model incorporating CO_2 dissolution, competitive adsorption, stress sensitivity and relative-permeability hysteresis, and evaluated fracture configurations and injection timing. Liu et al. [36] combined dissolution and geochemical modeling with an orthogonal design to assess how injection scheme, injection and production rates, and shut-in conditions affect both gas recovery and CO_2 storage. Related methods for optimizing recovery and storage have also been developed for CO_2 huff-and-puff in tight oil reservoirs [37].

Building on these studies, the question addressed here is how transport and flow properties influence the recovery–storage balance in a converted tight gas well group

when both the depletion state and pressure-limited CO_2 delivery are considered. Recovery during the injection stage alone cannot establish the gain over continued depletion, and the specified injection rate does not necessarily represent the rate actually achieved. A consistent assessment therefore requires matched depletion references, common evaluation times and explicit accounting of actual CO_2 injection.

To address this question, a multicomponent numerical model of an actual seven-well group in the eastern Sulige gas field was developed. The study provides three connected analyses. First, dissolution, adsorption, diffusion, threshold pressure gradient and stress sensitivity are compared in the same heterogeneous model under common well controls, with changes in actual injection considered when interpreting CH_4 recovery and net CO_2 storage. Second, recovery during injection and cumulative recovery over the development period are distinguished; for the multifactor and supplementary cases, recovery increments are evaluated against continued depletion at the same producer bottom-hole pressure and evaluation time. Third, specified injection rate, conversion pressure and producer bottom-hole pressure are jointly screened through a three-factor five-level L25 orthogonal design and four supplementary simulations. The actual injected CO_2 mass under the injector pressure limit is used to interpret the recovery and storage responses and support selection of an operating compromise. These analyses clarify how flow restrictions and development history affect CO_2-EGR scheduling for the studied tight gas well group.

2. Model Setup and Case Design

2.1. Study Area and Well-Group Model

The study area lies in the eastern Sulige gas field, Ordos Basin. The target intervals are the He-8 member of the Lower Shihezi Formation and the Shan-1 member of the Shanxi Formation. The well group consists of the central well WELL-1 and six surrounding producers, WELL-2 to WELL-7, of which WELL-7 is horizontal. The central well produces during the depletion stage and is later converted to a CO_2 injector. The main reservoir parameters are listed in Table 1.

The well group covers an area of 2.99 km^2 with an average net pay thickness of 15.3 m. The areal grid size is 25 m × 25 m, the average layer thickness is 0.50 m, and the model contains 162,232 active blocks. The average porosity is 10.43% and the average permeability is 0.59 mD, with vertical permeability set to 0.1 times the horizontal value. The initial reservoir pressure is 27.7 MPa, the reservoir temperature is 98 °C, and the initial water saturation is 41.04%. The three-dimensional distributions of permeability and porosity are shown in Figure 1. Both properties are patchy in plan view and differ between layers. The simulation starts when the well group is put on depletion. The porosity and permeability fields were adopted from an existing geological model in which the spatial distributions were obtained by interpolating well-log-derived property data. Only this single spatial realization was used in the simulations; alternative geological realizations were not evaluated, and the uncertainty associated with the interpolated property fields was not systematically quantified.

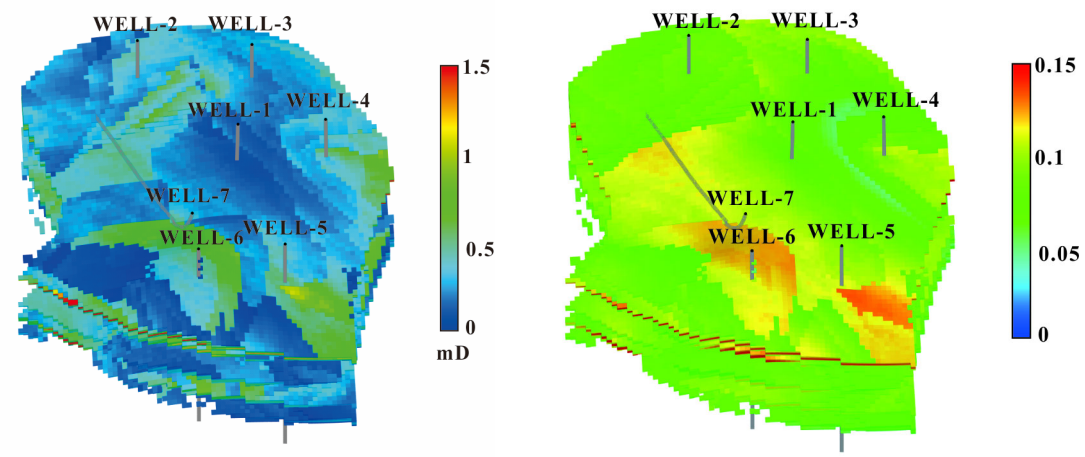
Closed (no-flow) boundary conditions were applied to all lateral, top, and bottom boundaries of the numerical model. No external aquifer support or fluid exchange with formations outside the model domain was included, and the injection and production wells were the only sources and sinks of mass.

The model was constructed from the existing geological model and actual well configuration, but it was not history matched against historical production or reservoir pressure data from the investigated well group. The results therefore provide a comparative assessment of the simulated cases, and their field-specific predictive accuracy has not been established.

https://doi.org/10.3390/en19235762

Table 1. Main reservoir parameters of the well group.

Parameter	Value	Unit
Number of active grid blocks	162,232	–
Areal grid size	25 × 25	m
Average layer thickness	0.50	m
Areal extent	2.99	km^2
Average net pay thickness	15.3	m
Effective pore volume	4.78×10^6	m^3
Average porosity	10.43	%
Average permeability	0.59	mD
Initial reservoir pressure	27.7	MPa
Reservoir temperature	98	°C
Initial water saturation	41.04	%



(**a**) (**b**)

Figure 1. Three-dimensional distribution of reservoir properties in the well-group model: (**a**) permeability (mD); (**b**) porosity (dimensionless).

2.2. Fluid Components and Phase Behavior

A ten-component fluid model was built with N_2, CO_2, CH_4, C_2, C_3, i-C_4, n-C_4, i-C_5, n-C_5 and C_6. The initial gas uses the representative average molar composition of the target area (Table 2). The formation water has a total salinity of 12.34 g/L and is of $CaCl_2$ type. The hydrocarbon components and N_2 are treated as insoluble in water, CO_2 partitions between the gas and water phases, and vaporization of water is not considered.

Table 2. Representative molar composition of the natural gas used in the model.

Component	Mole Fraction (%)
N_2	1.87
CO_2	0.83
CH_4	91.52
C_2H_6	4.09
C_3H_8	0.82
i-C_4H_{10}	0.19
n-C_4H_{10}	0.20
i-C_5H_{12}	0.12
n-C_5H_{12}	0.06
C_6	0.31

Gas-phase behavior and fugacity are computed with the Peng–Robinson (P–R) equation of state [38], written for a mixture as

$$p = \frac{RT}{v - b_m} - \frac{a_m(T)}{v^2 + 2b_m v - b_m^2} \tag{1}$$

where p is pressure, Pa; T is absolute temperature, K; v is molar volume, m³/mol; R is the universal gas constant, 8.314 J/(mol·K); and $a_m(T)$ and b_m are the attraction and co-volume parameters of the mixture, obtained from the van der Waals mixing rules:

$$a_m(T) = \sum_{i=1}^{N_c}\sum_{j=1}^{N_c} x_i\, x_j \sqrt{a_i(T)a_j(T)}\left(1 - k_{ij}\right), \qquad b_m = \sum_{i=1}^{N_c} x_i\, b_i \tag{2}$$

where x_i is the mole fraction of component i in the phase considered and $N_c = 10$; $a_i(T)$ and b_i are pure-component parameters determined from the critical temperature, critical pressure, acentric factor and the temperature-correction function; and k_{ij} is the binary interaction parameter. Critical properties, acentric factors and binary interaction parameters are taken from the component library of the simulator, the volume-shift parameters are set to zero, and gas viscosity is computed with the Lohrenz–Bray–Clark correlation [39].

2.3. Mathematical Model of Multicomponent Gas–Water Flow

The model is based on the following assumptions. (1) The reservoir fluid consists of a gas phase with ten components and a water phase containing water and dissolved CO_2. (2) Flow in the porous medium obeys component conservation and the generalized Darcy law, with the threshold pressure gradient and stress sensitivity taken into account. (3) Gas components can adsorb on the rock surface, and the adsorbed amount is controlled by partial pressure. (4) Molecular diffusion of CO_2 in the gas phase follows Fick's law. (5) The reservoir is isothermal.

2.3.1. Component Conservation Equations

For gas component i (i = 1, …, N_c), the molar balance includes storage in the pore fluid and in the adsorbed phase, and fluxes by convection and diffusion [40]:

$$\frac{\partial}{\partial t}\left[\phi \sum_{\alpha} S_\alpha\, c_\alpha x_{i,\alpha} + (1-\phi)\rho_r q_{i,\mathrm{ads}}\right] + \nabla \cdot \sum_{\alpha} \left(c_\alpha x_{i,\alpha} \mathrm{u}_\alpha + \mathrm{J}_{i,\alpha}\right) = q_{i,\mathrm{w}} \tag{3}$$

where α denotes the flowing phase (α = g and w for gas and water); ϕ is porosity; S_α is phase saturation; c_α is phase molar density, mol/m³; $x_{i,\alpha}$ is the mole fraction of component i in phase α; ρ_r is rock density, kg/m³; $q_{i,ads}$ is the adsorbed amount per unit mass of rock, mol/kg; u_α is the Darcy velocity, m/s; $J_{i,\alpha}$ is the diffusive molar flux, mol/(m²·s); and $q_{i,w}$ is the well source–sink term per unit volume, mol/(m³·s). The mole fractions of the ten gas components and of H_2O and CO_2 in the water phase satisfy the closure constraints.

$$S_g + S_w = 1, \sum_{i=1}^{N_c} x_{i,g} = 1, x_{H_2O,w} + x_{CO_2,w} = 1 \tag{4}$$

2.3.2. Flow Equations and Corrections for Tight Reservoirs

Phase velocities are given by the generalized Darcy law:

$$\mathrm{u}_\alpha = -\frac{\mathrm{K}\, k_{r\alpha}}{\mu_\alpha}\left(\nabla p - \rho_\alpha g \nabla z\right) \tag{5}$$

where K is the absolute permeability tensor, m^2; $k_r\alpha$ is the relative permeability of phase α; μ_α is phase viscosity, Pa·s; p is pore pressure, Pa; ρ_α is phase mass density, kg/m^3; g is gravitational acceleration, m/s^2; and z is the vertical coordinate, m.

Gas–water flow is described by relative permeability curves, and the same curves are used in all cases. This representative curve set was compiled from experimental measurements on several core samples from the same stratigraphic interval and block as the investigated well group, providing an experimental basis relevant to the target reservoir. Figure 2 gives the gas–water relative permeability curves; the gas data are converted to the water-saturation axis through $S_w = 1 - S_g$.

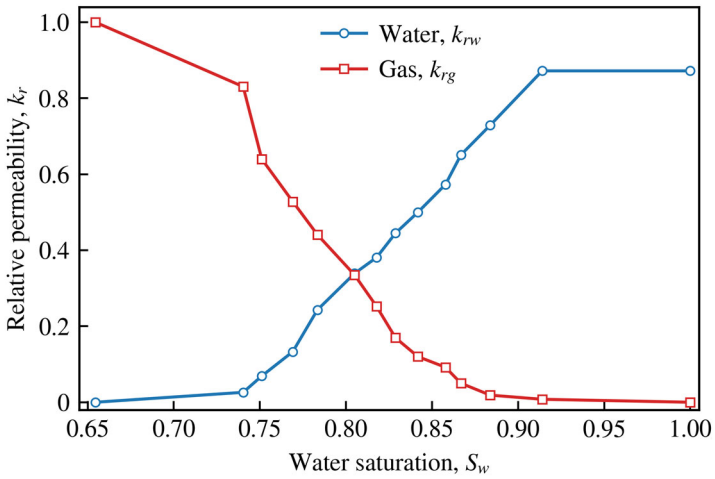


Figure 2. Gas–water relative permeability curves.

Gas flow in tight reservoirs is nonlinear at small pressure differences because of the threshold pressure gradient [29–31]. The model represents this effect through direction-dependent threshold pressures assigned to the grid connections. When the absolute pressure difference between two neighboring blocks exceeds the threshold of that connection, only the part above the threshold drives flow; otherwise, the effective driving pressure difference is zero:

$$\Delta p_{eff} = sgn(\Delta p)max(|\Delta p| - p_{th}, 0) \quad (6)$$

where Δp is the pressure difference between neighboring blocks, MPa, and *pth* is the connection threshold pressure, MPa. The threshold pressure gradient and the connection threshold are related through the grid spacing, $p_{th} = G_{th}L$, with Gth in MPa/m and L in m. The reference TPG–permeability relation was based on existing laboratory data from the research project supporting this study. Nitrogen-flow experiments were conducted on five tight sandstone cores from the Sulige gas field, with permeabilities ranging from 0.032 to 2.462 mD, at a confining pressure of 55 MPa and a backpressure of 30 MPa. The curve corresponding to an irreducible water saturation of 45% was adopted as the experimental basis for the reference relation ($G_0 = 0.0104K^{-0.772}$) shown in Figure 3a, where (G_0) is in MPa/m and (K) is in mD. This relation was applied to the well-group model without further calibration of its coefficients against field data from the investigated well group. Multipliers of 0.8, 0.9, 1.0, 1.1 and 1.2 were applied to (G_0) solely for sensitivity analysis. The threshold pressure gradient was treated as a permeability-dependent physical parameter independent of grid spacing. The threshold pressure difference at each grid connection was calculated by multiplying the threshold pressure gradient by the distance between adjacent cell centers. Therefore, changes in grid spacing affect the threshold pressure difference at individual connections but do not change the prescribed threshold pressure gradient. However, a formal grid-refinement analysis was not performed in this

study, and the potential influence of grid resolution on the predicted gas recovery, CO_2 migration, and storage performance remains unquantified.

As pore pressure declines, the effective stress increases and pore throats deform, which lowers permeability [34,41]. The model uses a table of pressure-dependent multipliers, and the transmissibility in each direction is corrected as

$$T_d(p) = T_{d,0} m_d(p) \tag{7}$$

where T_d is the transmissibility in direction d; $T_{d,0}$ is the reference transmissibility before the multiplier is applied; and m_d is the dimensionless transmissibility multiplier. The same input curve is used in all directions and the pore-volume multiplier is unity. Although incomplete permeability recovery during repressurization has been observed experimentally, the present model adopts a single-valued pressure-dependent transmissibility relationship without explicitly representing irreversible permeability damage or hysteresis. This simplification was used to isolate the effect of stress-dependent flow capacity while maintaining consistent model settings. It may overestimate the recovery of flow capacity during CO_2 injection, and the resulting uncertainty should be considered when interpreting the simulation results. The input curves are given in Figure 3b, with S3 as the base curve. In the low-pressure range the multipliers of S2, S3, S4 and S5 decrease in that order, and the multiplier of the case without stress sensitivity is unity throughout.

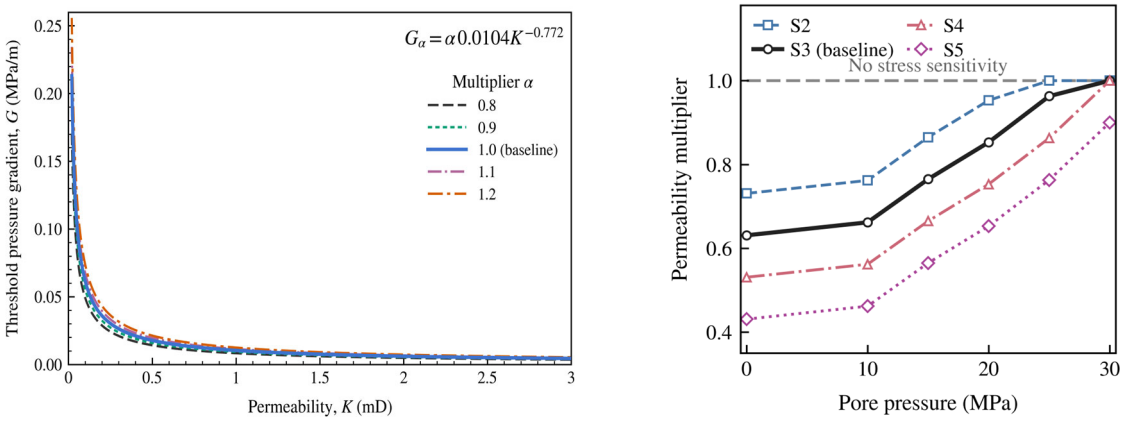


Figure 3. Input curves for the threshold pressure gradient and stress sensitivity: (**a**) threshold pressure gradient versus permeability, with the 1.0 multiplier as the base case; (**b**) pressure-dependent transmissibility multiplier, with S3 as the base curve.

2.3.3. Adsorption of Gas Components

Tight sandstone adsorbs both CH_4 and CO_2. The adsorbed storage of the two components is described separately, and the adsorbed amount of each component is computed from its partial pressure in the gas phase with the Langmuir isotherm [42]:

$$q_{i,ads} = q_{L,i} \frac{y_i p}{p_{L,i} + y_i p} \tag{8}$$

where $q_{L,i}$ is the saturated adsorption capacity of component i, mol/kg; $p_{L,i}$ is its Langmuir pressure, Pa; y_i is its mole fraction in the gas phase; and $y_i p$ is its partial pressure. Isothermal adsorption experiments were carried out at 100 °C and 0–27 MPa. Fitting Equation (8) to the measurements gives a saturated adsorption capacity and a Langmuir pressure of 1.74 mg/g and 17.55 MPa for CH_4, and of 7.78 mg/g and 22.07 MPa for CO_2; the capacity is expressed as adsorbed gas mass per unit rock mass and converted through

the molar mass. The measured partial-pressure–adsorption relations of CO_2 and CH_4 are entered as independent-component adsorption tables, and the other components are treated as non-adsorbing. These independent component tables account for the dependence of adsorption on each component's partial pressure but do not explicitly represent competition between CH_4 and CO_2 for shared adsorption sites. This simplification may affect the predicted exchange between adsorbed and free gas and consequently the estimates of CH_4 recovery and reservoir CO_2 inventory; the magnitude of this uncertainty was not quantified. The Langmuir parameters fitted at 100 °C were adopted directly for the isothermal simulations at the reservoir temperature of 98 °C, because the two temperatures differ by only 2 °C. This treatment assumes that the measured isotherms remain representative over this narrow temperature interval; the uncertainty associated with this approximation was not quantified.

2.3.4. Dissolution of CO_2 in Formation Water

Partitioning of CO_2 between the gas and water phases is set by the equality of fugacity in the two phases. The gas-phase fugacity of CO_2 is obtained from the equation of state given in Equation (1), and the fugacity in the water phase is described by Henry's law [43]:

$$\varphi_{CO_2}\, y_{CO_2}\, p = f_{CO_2} = H_{CO_2}\, x_{CO_2,w} \tag{9}$$

where φ_{CO2} is the fugacity coefficient of CO_2 in the gas phase; f_{CO2} is the fugacity of CO_2, Pa; $x_{CO2,W}$ is the mole fraction of CO_2 in the water phase; and H_{CO2} is the Henry constant, which has the same dimension as fugacity. The pressure dependence of the Henry constant is corrected following Li and Nghiem [43]:

$$H_{CO_2}(p,T) = H_{CO_2,ref}(T)\, exp\left[\frac{v^{\infty}\,(p - p_{ref})}{RT}\right] \tag{10}$$

where $H_{CO2,ref}$ is the Henry constant at the reference pressure p_{ref} and v^{∞} is the partial molar volume of CO_2 in water at infinite dilution. At the reservoir temperature of 98 °C the reference pressure is 5 MPa, the corresponding Henry constant is 532.25 MPa, and the partial molar volume at infinite dilution is 31.26 cm^3/mol. The CO_2 mole fraction in the water phase computed from these values is 0.51–1.70% over 5–45 MPa.

2.3.5. Diffusion in the Gas Phase

Injected CO_2 mixes with reservoir CH_4 near the displacement front. Molecular diffusion in this zone is described by an effective Fickian relation [17], and the diffusive molar flux of CO_2 in the gas phase is

$$J_{CO_2,g} = -\phi S_g c_g D_{eff} \nabla y_{CO_2} \tag{11}$$

where D_{eff} is the effective molecular diffusion coefficient, m^2/s, and y_{CO2} is the mole fraction of CO_2 in the gas phase. The coefficient was treated as constant within each simulation case, with a base value of 2.48×10^{-8} m^2/s. The baseline was taken from core-scale diffusion measurements conducted for the research project at 100 °C. The measured coefficients at 9, 18, and 27 MPa were 5.26×10^{-8}, 3.66×10^{-8}, and 2.48×10^{-8} m^2/s, respectively; the value measured at 27 MPa was adopted for the base case. The additional values of 0, 2.48×10^{-9}, 4.84×10^{-8}, and 2.48×10^{-7} m^2/s in Table 3 were prescribed solely for sensitivity analysis and were not additional measured values. The zero-diffusion case isolates the contribution of the modeled diffusion term, while the nonzero values explore sensitivity around the baseline; these settings do not define a measured range of reservoir diffusion coefficients. Mechanical dispersion was not explicitly included, and no velocity-dependent longitudinal or transverse dispersivity terms were specified. This

simplification may underestimate the physical broadening of the CO_2-CH_4 mixing zone, introducing uncertainty into predictions of CO_2 breakthrough, produced-gas composition and concentration-triggered well shut-in. The resulting effects on recovery and CO_2 storage depend on the reservoir heterogeneity and operating controls.

Table 3. Settings of the mechanism-property comparison cases.

Property	Base Setting	Compared Levels
Dissolution in water	Included	Excluded
Adsorption	Included	Excluded
Diffusion coefficient	2.48×10^{-8} m²/s	0, 2.48×10^{-9}, 2.48×10^{-8}, 4.84×10^{-8}, 2.48×10^{-7} m²/s
Threshold pressure gradient	Multiplier 1.0, Figure 3a	Multipliers 0.8, 0.9, 1.0, 1.1, 1.2
Stress sensitivity	Curve S3, Figure 3b	S2, S3, S4, S5 and no stress sensitivity

The numerical simulations were performed using the commercial compositional reservoir simulator tNavigator (version 23.4, Rock Flow Dynamics,Moscow, Russia). The governing component conservation equations were discretized spatially using a cell-centered finite-volume method, with upstream weighting for phase mobilities. An implicit time-integration scheme with adaptive time stepping was employed, and the resulting nonlinear algebraic equations were solved using Newton–Raphson iterations. Fluid phase behavior was calculated using the Peng–Robinson equation of state, as described in Section 2.2. The computational grid, initial reservoir properties, and injection–production controls are specified in Sections 2.1 and 2.4.

2.4. Case Design

2.4.1. Continued Depletion Versus CO_2 Flooding

Two cases were set up: continued depletion and base CO_2 flooding. During the first 10 years of depletion both cases use the same well control. After 10 years the central well of the CO_2 flooding case is converted to an injector with a bottom-hole pressure limit of 45 MPa, while the central well of the depletion case keeps producing. A producer is shut in when the CO_2 mole fraction of its produced gas reaches 20%. This threshold was selected with reference to the field conditions of the investigated well group, taking into account the conversion of an existing production well to CO_2 injection and operational concerns about CO_2-related pipeline corrosion. The same operational cutoff was applied to all simulation cases. The time of conversion in the base case is taken as the common reference time t = 0; the main and extended evaluation times are t = 22 years and t = 27 years, that is, years 32 and 37 of the whole development period. Cases in which conversion is triggered by pressure are evaluated at the same development times, so that their actual injection durations differ with the conversion time.

2.4.2. Single-Factor Sensitivity Analysis

The single-factor analysis of mechanism properties changes dissolution, adsorption, diffusion coefficient, threshold pressure gradient and stress sensitivity one at a time from the base CO_2 flooding case, keeping all other conditions fixed. The settings are listed in Table 3, and the input relations for the threshold pressure gradient and stress sensitivity are shown in Figure 3. The single-factor analysis of the injection–production strategy covers injection pressure, specified CO_2 mass injection rate, conversion pressure of the central well and producer bottom-hole pressure, each at five levels (Table 4). The property cases are evaluated up to t = 22 years and the strategy cases up to t = 27 years.

Table 4. Levels of the injection–production parameters used in the single-factor analysis.

Factor	Unit	Levels
Injection pressure	MPa	35, 40, 43, 44, 45
Specified injection rate A	t/d	20, 40, 60, 80, 100
Conversion pressure of the central well B	MPa	10, 8, 6, 4, 3
Producer bottom-hole pressure (BHP) C	MPa	3, 4, 5, 6, 7.5

2.4.3. Multifactor Orthogonal Design and Supplementary Cases

A three-factor five-level L25 orthogonal design was used to study the combined effect of the specified injection rate A, the conversion pressure of the central well B and the producer bottom-hole pressure C. The 25 combinations are listed in Table 5. Each level of every factor appears five times, and the level pairs of any two factors are balanced. A continued-depletion case was run for each producer pressure level to compute the incremental recovery of CO_2 flooding over depletion.

The central well WELL-1 is converted from production to CO_2 injection when its bottom-hole pressure drops to B, so the conversion time is triggered by pressure and differs between cases. The six surrounding producers operate at the specified bottom-hole pressure C, which is not applied to the central well. Factor A is the specified injection rate; the actual rate and the cumulative injected mass are read from the simulation results. The bottom-hole pressure limit of the injector is 45 MPa, and a producer is shut in when the CO_2 mole fraction of its produced gas reaches 20%.

The cumulative CH_4 recovery factor and the incremental recovery over the matched depletion case were taken as responses. The mean response of each level of each factor was computed, and the share of the main-effect sum of squares in the total sum of squares was used to compare the influence of the factors [37]. An additive main-effect prediction built from the level means was used to screen candidate combinations, which were then checked by supplementary simulations. The design has no replicates, so the residual term contains unseparated non-additive variation; it is not interpreted as pure random error and is not used to judge statistical significance.

Four supplementary cases were added to the 25 orthogonal cases: V1 = (80 t/d, 3 MPa, 7.5 MPa), V2 = (20 t/d, 3 MPa, 7.5 MPa), V3 = (40 t/d, 4 MPa, 7.5 MPa) and V4 = (40 t/d, 3 MPa, 6 MPa), where the values in parentheses are A, B and C. Case R10 = (40 t/d, 3 MPa, 7.5 MPa) serves as the local reference for examining changes in the specified injection rate, the conversion pressure and the producer pressure. The final selection is based on the cumulative CH_4 recovery factor and the CO_2 storage obtained directly from the simulations.

Table 5. Parameter combinations of the three-factor five-level L25 orthogonal design.

Case	A Specified Injection Rate/(t/d)	B Conversion Pressure/MPa	C Producer BHP/MPa
R1	20	10	7.5
R2	20	8	6
R3	20	6	5
R4	20	4	4
R5	20	3	3
R6	40	10	6
R7	40	8	5
R8	40	6	4
R9	40	4	3
R10	40	3	7.5

R11	60	10	5
R12	60	8	4
R13	60	6	3
R14	60	4	7.5
R15	60	3	6
R16	80	10	4
R17	80	8	3
R18	80	6	7.5
R19	80	4	6
R20	80	3	5
R21	100	10	3
R22	100	8	7.5
R23	100	6	6
R24	100	4	5
R25	100	3	4

2.5. Performance Indicators

Development performance is evaluated by the cumulative CH_4 recovery factor and the CO_2 storage. The cumulative CH_4 recovery factor R_{CH4} is computed from the decrease in CH_4 in place:

$$R_{CH_4}(t) = 100\frac{N_{CH_4,0} - N_{CH_4}(t)}{N_{CH_4,0}} \quad (12)$$

where $N_{CH4,0}$ is the original CH_4 in place expressed in moles and $N_{CH4}(t)$ is the remaining amount at time t. This indicator measures the decrease in CH_4 in place over the whole development period. The property comparison uses the incremental CH_4 recovery within 22 years after conversion, defined as the decrease in CH_4 in place during that period divided by the original amount in place, which reflects recovery during the CO_2 flooding stage; the indicator also carries the effect of the state of development reached before conversion.

The incremental recovery $\Delta R_{CH4,i}$ is the difference in cumulative recovery factor between a CO_2 flooding case and the continued-depletion case at the same producer pressure, expressed in percentage points (pp):

$$\Delta R_{CH_4,i}(t) = R_{CH_4,i}(t) - R_{dep,C_i}(t) \quad (13)$$

where C_i is the producer pressure of case i and $R_{dep,Ci}$ is the recovery factor of the corresponding depletion case. This indicator measures the gas recovery gain obtained by converting the central well to CO_2 injection.

The net CO_2 storage ΔM_{CO2} is the net increase in the total CO_2 in the reservoir relative to a specified reference time:

$$\Delta M_{CO_2}(t) = \left[N_{CO_2}(t) - N_{CO_2,ref}\right]\frac{44.01}{1000} \quad (14)$$

where N_{CO2} is the total amount of CO_2 in the reservoir, including the free gas, the dissolved and the adsorbed fractions, kmol; $N_{CO2,ref}$ is its value at the reference time; and 44.01 kg/kmol is the molar mass of CO_2, with the result converted to tonnes. This indicator describes the net change in the CO_2 inventory during the simulated development period. This indicator represents the net change in reservoir CO_2 inventory at a specified evaluation time rather than the long-term geological storage capacity. The present assessment does not explicitly evaluate post-injection CO_2 migration, caprock integrity, potential leakage pathways, or long-term containment. Therefore, the calculated CO_2 inventory increase should be interpreted as a measure of storage performance within the

simulated development period, rather than as the amount of CO_2 that can be permanently and safely stored.

Three objectives are considered in the selection of cases: gas recovery priority, storage priority and a balance of the two. Gas recovery priority uses the cumulative CH_4 recovery factor, storage priority uses the CO_2 storage, and the balanced selection compares both indicators. For the balanced selection, the gains and losses in both indicators were assessed relative to the best-performing cases for the individual objectives, providing an engineering comparison without a weighted objective function or economic optimization. The incremental recovery measures the gas recovery gain of CO_2 flooding over the matched depletion case. For the supplementary cases, the incremental CH_4 produced relative to the matched depletion case at the same evaluation time is also divided by the cumulative injected CO_2 mass, which gives the incremental CH_4 per unit of injected CO_2 (kmol/t).

3. Results and Discussion

3.1. CO_2 Flooding Compared with Continued Depletion

Figure 4 shows the cumulative CH_4 recovery factor of the base CO_2 flooding case and of continued depletion. After 10 years of depletion the cumulative recovery factor of the well group is 24.37%, and CH_4 in place has fallen from the original 2.52×10^7 kmol to 1.91×10^7 kmol. The recovery curve has flattened by this time, which indicates that the incremental recovery from further depletion under the given well control is becoming small. The two cases separate after the central well is converted. At 22 years after conversion the cumulative CH_4 recovery factor of the CO_2 flooding case reaches 29.00% against 25.88% for continued depletion, a difference of 3.12 percentage points. This corresponds to about 7.86×10^5 kmol of additional CH_4, or 12.05% of the cumulative production of the depletion case. Within the 22 years after conversion the incremental recovery of the two cases is 4.63% and 1.51%, so CO_2 flooding raises the production of this stage to more than three times that of depletion.

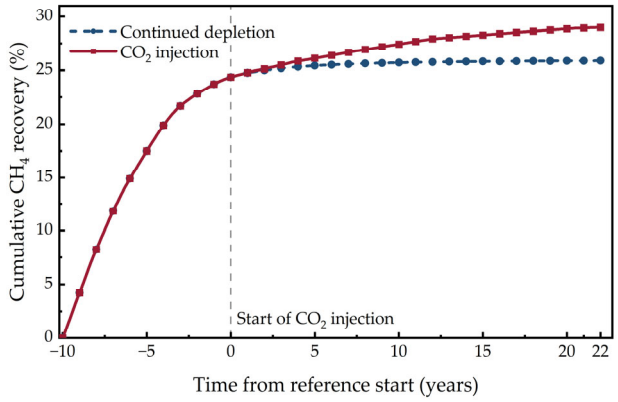


Figure 4. Cumulative CH_4 recovery factor versus time for the base CO_2 flooding case and for continued depletion. The vertical line marks the conversion of the central well; the two cases use the same well control before conversion.

The gain from CO_2 flooding does not appear immediately after conversion. Six months after conversion the cumulative recovery factor of the CO_2 flooding case is still about 0.01 percentage points below that of continued depletion, and it overtakes the depletion case only ten months after conversion. This lag is consistent with the loss of production from the central well and the gradual response of the surrounding producers to injection; the crossover of the cumulative curves shows that from that time on the gain

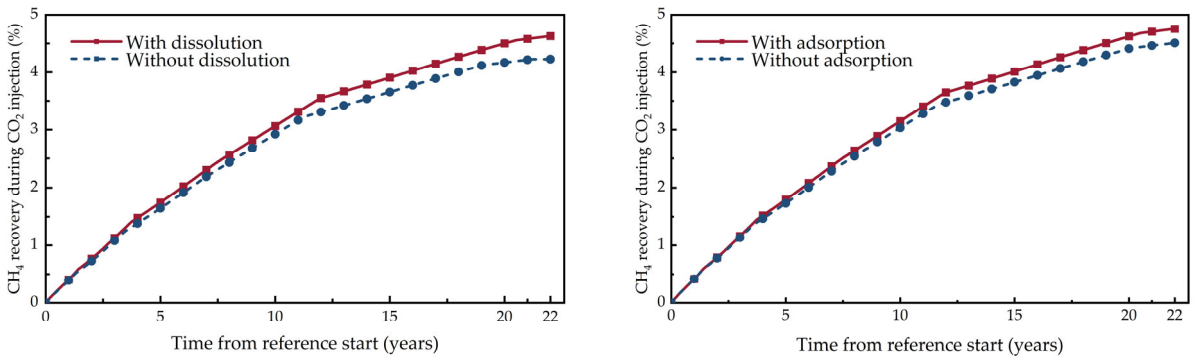
at the producers offsets the loss at the central well. Pressure propagation under low permeability may contribute to this process, and its relative role needs to be assessed from the interwell pressure response.

3.2. Effect of Mechanism Properties on CO_2 Flooding

3.2.1. Dissolution and Adsorption

Dissolution of CO_2 in formation water raises both CH_4 recovery and CO_2 storage (Figure 5a). With dissolution included, the incremental CH_4 recovery within 22 years after conversion rises from 4.23% to 4.63%, an increase of 0.40 percentage points, and the CO_2 storage rises from 21.35 × 10^4 t to 21.87 × 10^4 t, an increase of 0.52 × 10^4 t. Dissolution moves part of the CO_2 into the water phase and changes the component distribution between the two phases. The differences above are the combined result of dissolution, injection and production under fixed well control, and the change in cumulative quantities alone does not quantify the drop in near-well pressure or the displacement contribution separately.

The effect of adsorption is smaller but acts in the same direction (Figure 5b). Using the original CH_4 in place of the case without adsorption as a common denominator, the incremental CH_4 recovery within 22 years after conversion rises from 4.51% to 4.76%, an increase of 0.25 percentage points, and the CO_2 storage rises from 21.82 × 10^4 t to 21.87 × 10^4 t, an increase of 491 t. Including adsorption changes both the initial CH_4 storage and the amount desorbed during production, so the difference reflects the combined recovery response to the adsorption setting rather than CO_2 competitive displacement alone. The small difference in total CO_2 between the two cases likewise does not mean that the adsorbed CO_2 fraction is small; the share of each storage form has to be determined from the component inventories.



(**a**) (**b**)

Figure 5. Effect of dissolution and adsorption on the incremental CH_4 recovery within 22 years after conversion: (**a**) with and without CO_2 dissolution in formation water; (**b**) with and without CO_2/CH_4 adsorption.

3.2.2. Diffusion and Threshold Pressure Gradient

Over the range examined, the diffusion coefficient gives the largest recovery response among the transport parameters (Figure 6a,b). When the diffusion coefficient increases from 0 to 2.48 × 10^{-7} m^2/s, the incremental CH_4 recovery within 22 years after conversion rises from 2.26% to 5.93%, an increase of 3.66 percentage points and about 2.62 times the value of the case without diffusion. Over the same period the cumulative CO_2 injection rises from 11.96 × 10^4 t to 24.05 × 10^4 t, a factor of 2.01, and the CO_2 storage rises from 11.89 × 10^4 t to 23.95 × 10^4 t. Incremental recovery and cumulative injection increase together as the diffusion coefficient changes, which shows that the effect of this parameter is coupled with the injection process under the pressure constraint. The incremental recovery curve

of the case without diffusion flattens about nine years after conversion. These differences are the combined response under a given well control, and the contributions of production from low-permeability regions, of the widening of the mixing zone and of the change in shut-in time cannot be separated from the cumulative recovery and injection curves alone.

The threshold pressure gradient also has a marked effect on recovery and injection, and it acts over the whole development period (Figure 6c,d). With the threshold set to 0.8, 0.9, 1.0, 1.1 and 1.2 times the base value, the incremental CH_4 recovery within 22 years after conversion is 6.15%, 5.37%, 4.63%, 3.39% and 2.08%, a maximum difference of 4.07 percentage points and the largest response among the settings examined. At conversion the cumulative recovery factors of the 0.8 and 1.2 cases are 28.34% and 20.78%, and at 22 years after conversion they are 34.49% and 22.86%, which shows that the threshold affects recovery during both the depletion and the CO_2 flooding stages. The cumulative CO_2 injection falls from 33.47×10^4 t at 0.8 times to 13.13×10^4 t at 1.2 times, and the CO_2 storage falls from 33.34×10^4 t to 13.14×10^4 t. A higher threshold pressure gradient raises the pressure difference required for flow across a grid connection, so both recovery and injection decrease as the threshold increases under the given injection pressure limit.

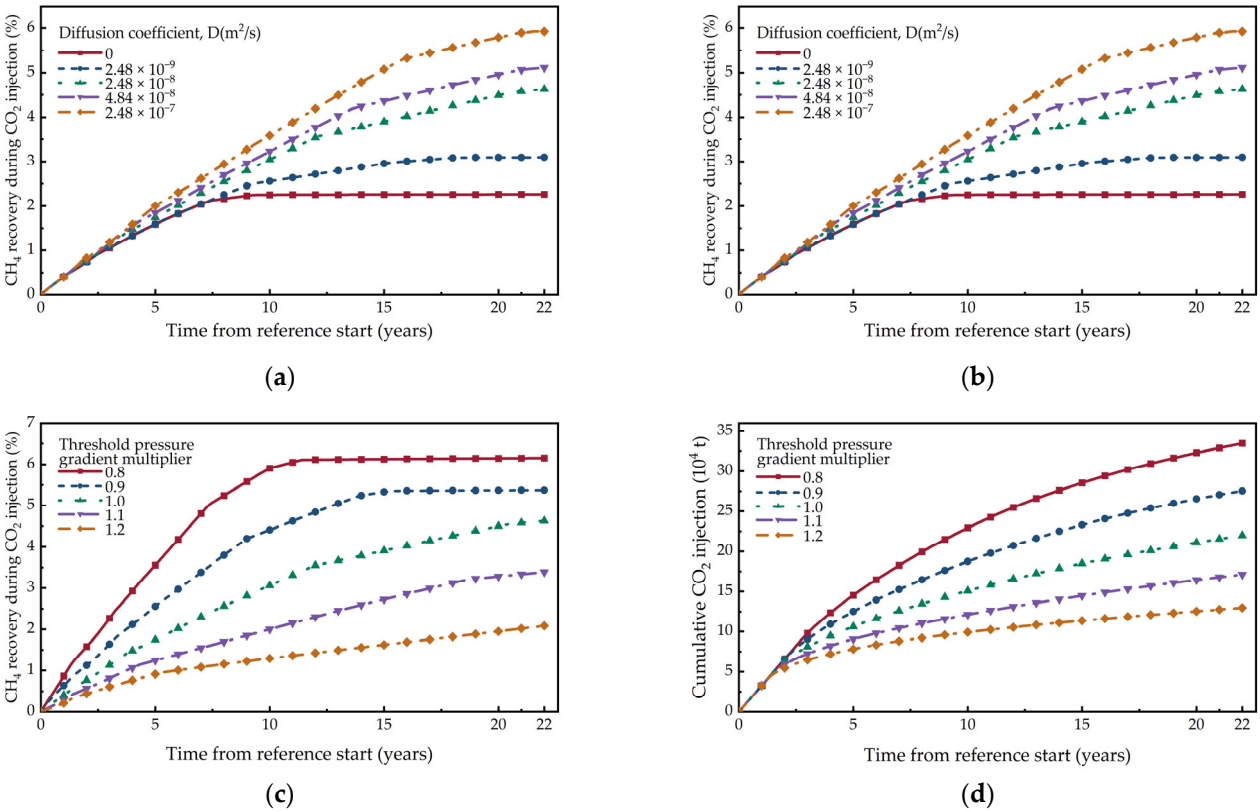


Figure 6. Effect of the diffusion coefficient and the threshold-pressure-gradient multiplier on incremental CH_4 recovery and cumulative CO_2 injection within 22 years after conversion: (**a**,**b**) diffusion coefficient (D, m^2/s); (**c**,**d**) threshold-pressure-gradient multiplier.

3.2.3. Stress Sensitivity

Stress sensitivity ranks the cases differently for stage recovery and for full-cycle recovery (Figure 7). The recovery shown in Figure 7 represents CH_4 produced during the injection stage, normalized by the original CH_4 in place, whereas cumulative recovery includes both depletion and injection. A higher injection-stage recovery may therefore coexist with lower cumulative recovery when it does not compensate for the lower production before conversion. The incremental CH_4 recovery within 22 years after

conversion is 4.95%, 4.84%, 4.63%, 4.49% and 4.34% for S5, S4, S3, S2 and the case without stress sensitivity, so stronger stress sensitivity gives higher stage recovery. The cumulative recovery factors at 22 years after conversion are 28.87%, 29.01%, 29.00%, 29.00% and 29.08%, with the case without stress sensitivity highest. The reason lies in the recovery reached before conversion. At conversion the cumulative recovery factors of S5 and of the case without stress sensitivity are 23.92% and 24.74%; S5 produces 0.83 percentage points less because of the larger permeability loss during depletion, and therefore has more CH_4 left in place at conversion. Within the 22 years after conversion S5 produces 0.62 percentage points more, which does not close the earlier gap, and its cumulative recovery factor ends 0.21 percentage points lower. Judging stress sensitivity from stage recovery alone therefore overstates its benefit for CO_2 flooding, and its effect must be assessed over both the depletion and the flooding stages. The CO_2 storage does not change monotonically with the curve number either: S4 and S5 give about 22.55×10^4 t and 21.76×10^4 t, and this also reflects the different multipliers of the input curves at high pressure (0.90 for S5 at 30 MPa against 1.00 for the others).

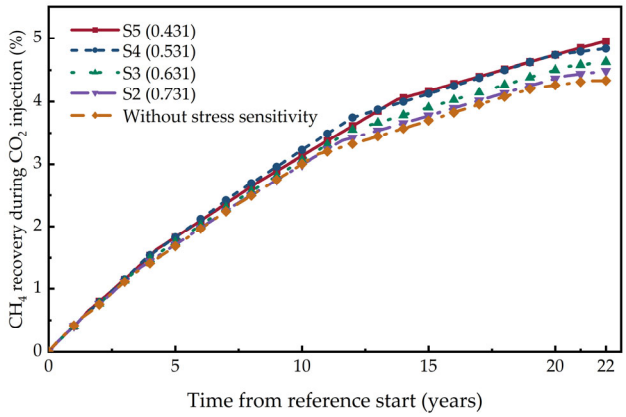


Figure 7. Injection-stage CH_4 recovery within 22 years after conversion for different stress-sensitivity curves.

Table 6 summarizes the property comparison. Over the ranges set here, diffusion and the threshold pressure gradient change recovery by 3.66 and 4.07 percentage points, clearly more than dissolution and adsorption at 0.40 and 0.25 percentage points. The net CO_2 inventory increase in the property cases follows the actual injected volume. Because this indicator also includes the change in native CO_2, its ratio to the cumulative injection should not be read as the retained fraction of the injected CO_2. The comparison describes the inventory response within the evaluation period and does not address long-term containment. For CO_2 flooding evaluation in this type of tight gas reservoir, the flow-capacity parameters of the reservoir, namely the threshold pressure gradient and stress sensitivity, are therefore as important as the transport parameters, and CH_4 recovery, actual injection and CO_2 storage should be examined together rather than through the recovery factor alone.

Table 6. Simulation-derived injection-stage CH_4 recovery and CO_2 storage within 22 years after conversion for different mechanism settings.

Property	Compared Range	Injection-Stage CH_4 Recovery (%)	CO_2 Storage (10^4 t)	Main Response
Dissolution	With/without	4.63/4.23	21.87/21.35	Recovery and CO_2 inventory both increase
Adsorption	With/without	4.76/4.51	21.87/21.82	Recovery increases; CO_2 inventory changes little
Diffusion	D = 0→2.48 × 10^{-7} m^2/s	2.26→5.93	11.89→23.95	Recovery and actual injection increase together
Threshold pressure gradient	0.8→1.2 times	6.15→2.08	33.34→13.14	Recovery and actual injection both decrease
Stress sensitivity	S5→none	4.95→4.34	21.76→21.89	Stage and full-cycle rankings differ

Note: For the adsorption comparison, both recovery values are normalized by the initial CH_4 inventory of the case without adsorption.

3.3. Single-Factor Analysis of Injection–Production Parameters

3.3.1. Injection Pressure

A higher injection pressure raises both the cumulative CH_4 recovery factor and the cumulative CO_2 injection, but the recovery gain becomes smaller as the pressure increases (Figure 8a). When the injection pressure rises from 35 MPa to 45 MPa, the cumulative recovery factor at the main evaluation time (t = 22 years) rises from 26.24% to 28.99% and the cumulative CO_2 injection from 7.87 × 10^4 t to 22.40 × 10^4 t. Raising the pressure from 43 MPa to 44 MPa and then to 45 MPa adds only 0.31 and 0.20 percentage points of recovery, and at the extended evaluation time (t = 27 years) the difference between the 44 MPa and 45 MPa cases narrows to about 0.07 percentage points. The higher pressure increases the actual injected volume, but the gain in CH_4 recovery falls off, which shows that within this well control and evaluation period the additional injection does not produce a proportional increase in recovery; the total-quantity response alone does not separate pressure support from displacement. The 45 MPa case, the highest injection pressure computed here, gives the highest recovery factor of the group, but the benefit of raising the pressure further within 43–45 MPa is limited.

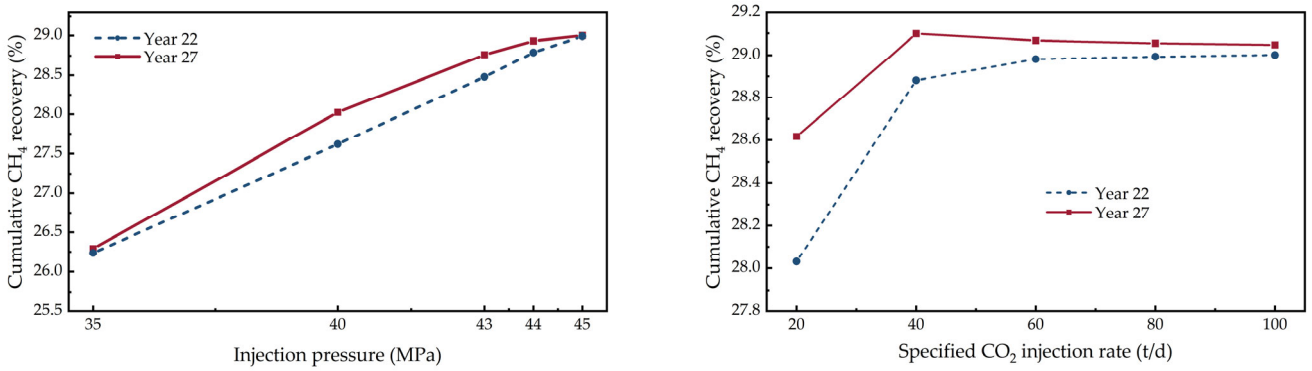


Figure 8. Cumulative CH_4 recovery factor: (**a**) different injection pressures; (**b**) different specified injection rates.

3.3.2. CO_2 Injection Rate

The effect of the specified injection rate on recovery also falls off, and the ranking of the cases changes with the evaluation period (Figure 8b). For specified rates of 20, 40, 60, 80 and 100 t/d the cumulative recovery factors at the main evaluation time are 28.03%, 28.88%, 28.98%, 28.99% and 29.00%, with only 0.02 percentage points between the 60 and 100 t/d cases. At the extended evaluation time the 40 t/d case reaches 29.10%, slightly above the 29.05% of the 100 t/d case.

The actual injection history explains this behavior (Figure 9). The cases with specified rates of 60, 80 and 100 t/d hold the specified rate for only about 3, 2 and 1 years; the bottom-hole pressure of the injector then reaches its limit, injection switches to pressure control, and the actual rates of all cases converge to a single curve that declines as reservoir pressure recovers. The 40 t/d case holds the specified rate for about 6 years and the 20 t/d case for almost the whole main evaluation period. During the last year of the extended evaluation period the actual mean injection rates of the 40, 60, 80 and 100 t/d cases are about 10.19, 9.11, 8.77 and 8.59 t/d, all far below the specified values. The injectivity of this well group is thus limited by the injection pressure limit together with the recovery of reservoir pressure. Cases with a high specified rate hold that rate only briefly, and after the switch to pressure control their actual rate declines, so their early recovery advantage weakens as production continues. Injection-rate cases must therefore be judged from the actual rate and the cumulative injected volume.

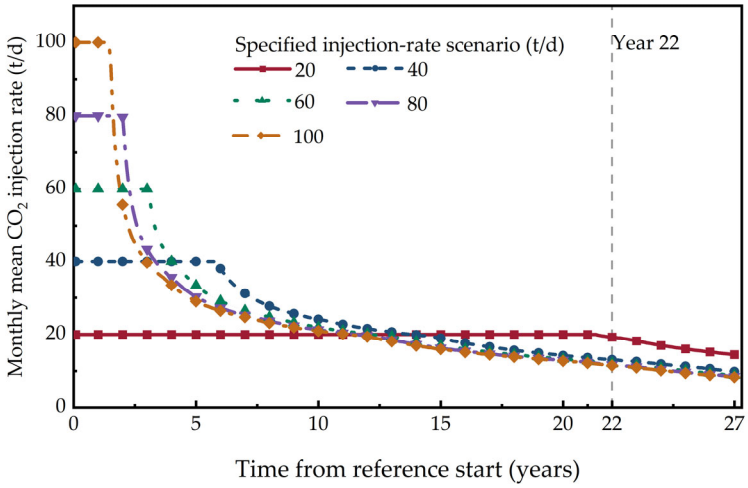


Figure 9. Monthly mean CO_2 mass injection rate versus time for different specified injection rates.

3.3.3. Timing of Conversion of the Central Well

Within the range examined, delaying conversion raises the cumulative CH_4 recovery factor (Figure 10a). When the conversion pressure of the central well falls from 10 MPa to 8, 6, 4 and 3 MPa, so that conversion takes place progressively later, the cumulative recovery factors at the main evaluation time are 27.50%, 27.77%, 28.03%, 28.36% and 28.52%. The 3 MPa case is 1.02 percentage points above the 10 MPa case and injects about 1.83×10^4 t more CO_2. At the same overall development time, a lower conversion pressure lengthens the production period of the central well and also changes the reservoir state at conversion and the actual injection duration. These results support the use of a low conversion pressure for this well group within the range examined, but they do not imply that later conversion is always better.

https://doi.org/10.3390/en19235762

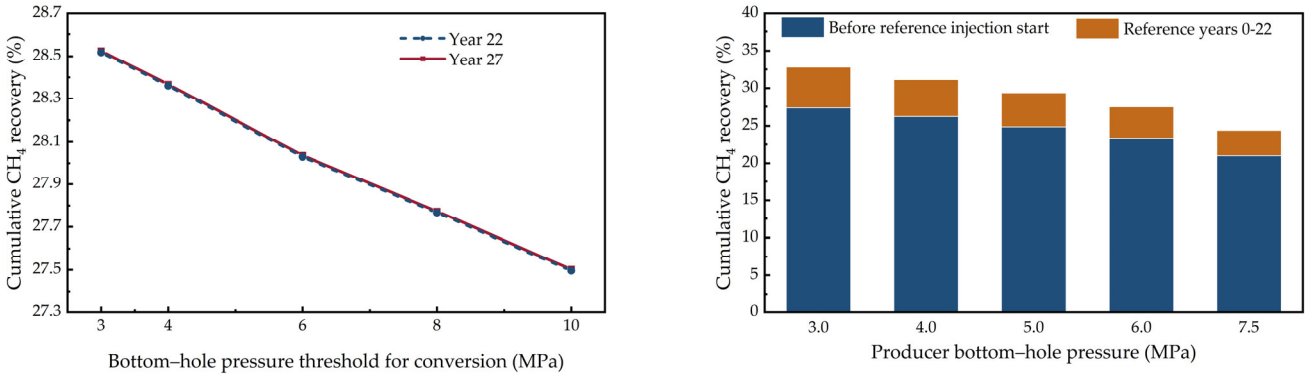


Figure 10. CH_4 recovery factor: (**a**) different conversion pressures; (**b**) different producer bottom–hole pressures.

3.3.4. Producer Bottom-Hole Pressure

For this well group and the parameter ranges examined, the producer bottom-hole pressure produces the largest response in cumulative recovery among the single factors (Figure 10b). When the pressure falls from 7.5 MPa to 3 MPa, the cumulative recovery factor at the main evaluation time rises from 24.40% to 32.81%, an increase of about 8.4 percentage points, of which 6.36 percentage points are accumulated before the reference time; the incremental recovery within the 22 years after the reference time rises from 3.42% to 5.46%. A lower producer pressure increases the drawdown, which extends the pressure-depleted area during depletion and increases the displacement pressure difference between injector and producers during CO_2 flooding, so recovery rises in both stages. Because the producer pressure acts over the whole development period, its cumulative effect is much larger than that of the injection parameters, which act only after conversion, and it should be given priority within the range of cases considered here.

3.4. Multifactor Orthogonal Analysis

For this well group and the factor levels examined, the main effects on the cumulative CH_4 recovery factor rank as producer bottom-hole pressure C, conversion pressure of the central well B and specified injection rate A (Table 7 and Figure 11). At the two evaluation times the main-effect sum-of-squares share of C is 97.98% and 97.75%, that of B is 1.95% and 2.09%, and that of A is 0.01% and 0.10%. The producer pressure acts during both the depletion and the flooding stages and therefore has the largest effect on full-cycle recovery; the weak main effect of the specified injection rate is consistent with the injection being limited by the pressure constraint in the middle and late stages. The cumulative recovery factors of the 25 cases range from 22.78% to 32.24% at the main evaluation time and from 23.07% to 32.42% at the extended evaluation time.

Every CO_2 flooding case is compared with the continued-depletion case at the same producer pressure; the depletion references are listed in Table 8. The incremental recovery of the 25 cases ranges from 0.46 to 3.49 percentage points at the main evaluation time and from 0.41 to 3.72 percentage points at the extended evaluation time, so all combinations examined show a gas recovery gain. When the incremental recovery is used as the response, the order of the factors remains C > B > A, but the share of C falls to 77.11% and 78.79%, the share of B rises to 22.06% and 19.77%, and the share of A is 0.16% and 0.90%. The cumulative recovery factor measures the full-cycle recovery level and the incremental recovery measures the gain over the matched depletion case, so the two indicators can rank the cases differently. Depletion recovery is low at high producer pressures, and a

case can show a large incremental recovery while its cumulative recovery factor remains below that of a low-pressure case.

In this balanced L25 design every level of A and B is paired once with every level of C. Removing the depletion reference, which varies only with C, leaves the main-effect sums of squares of A and B and the residual sum of squares unchanged, while the level differences of C and the total sum of squares change; the sum-of-squares shares therefore differ between the two responses.

Table 7. Calculated main-effect sum-of-squares shares (%) for the two evaluation responses. A: injection rate; B: conversion pressure; C: producer bottom-hole pressure. Bold values indicate the largest main-effect share in each row.

Evaluation Time	Response	A (%)	B (%)	C (%)	Residual (%)
t = 22 years	Cumulative CH_4 recovery factor	0.01	1.95	**97.98**	0.06
t = 22 years	Incremental recovery	0.16	22.06	**77.11**	0.68
t = 27 years	Cumulative CH_4 recovery factor	0.10	2.09	**97.75**	0.06
t = 27 years	Incremental recovery	0.90	19.77	**78.79**	0.54

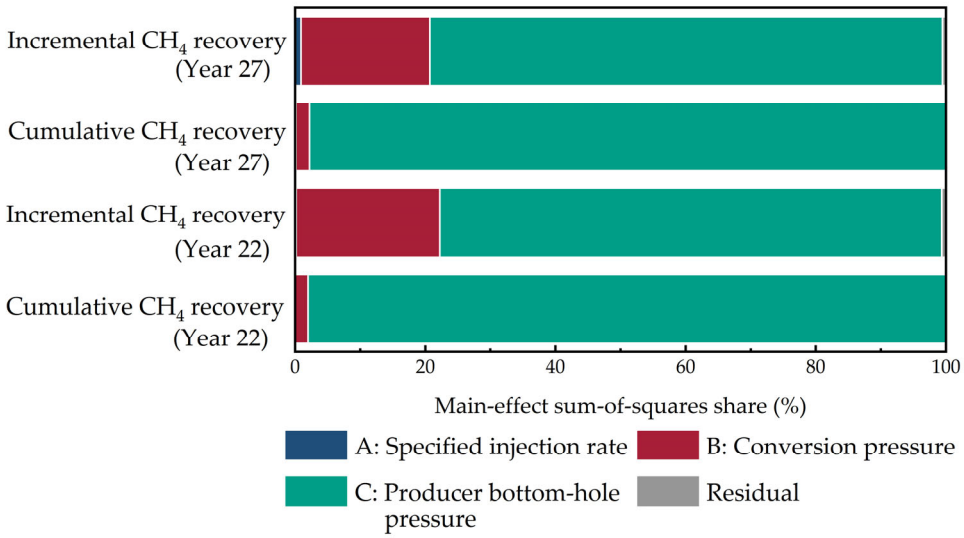


Figure 11. Main-effect sum-of-squares shares of the factors for the cumulative CH_4 recovery factor and for the incremental recovery.

Table 8. Cumulative CH_4 recovery factors from continued-depletion simulations at different producer bottom-hole pressures.

Producer BHP (MPa)	Recovery Factor at t = 22 Years (%)	Recovery Factor at t = 27 Years (%)
3	30.53	30.59
4	28.19	28.23
5	25.88	25.90
6	23.62	23.63
7.5	20.36	20.36

3.5. Comparison of the Supplementary Cases

Four supplementary cases were run from the reference case R10 = (40 t/d, 3 MPa, 7.5 MPa) to test local parameter changes and to check the additive main-effect prediction: V2 and V1 change the injection rate to 20 and 80 t/d, V3 raises the conversion pressure to 4

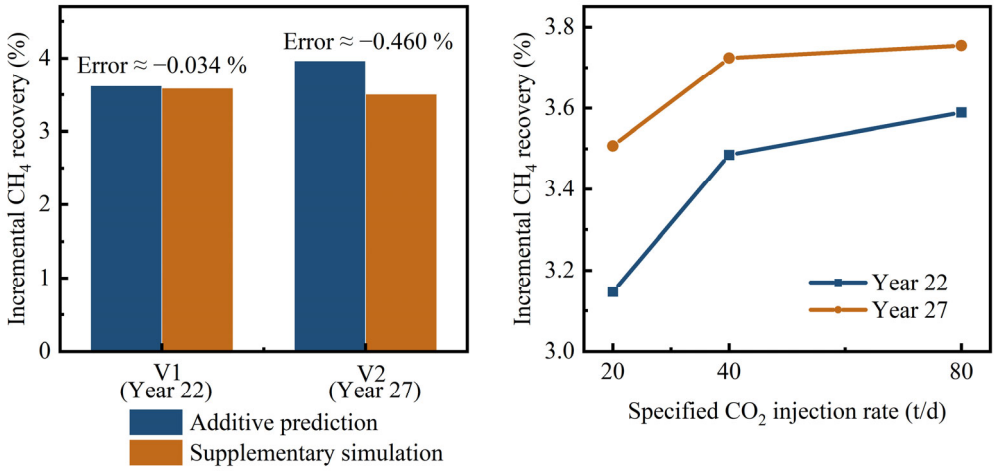
MPa, and V4 lowers the producer pressure to 6 MPa. The cumulative CH_4 recovery factor, the incremental recovery, the CO_2 storage and the incremental CH_4 per unit of injected CO_2 are listed in Table 9.

With the conversion pressure fixed at 3 MPa and the producer pressure at 7.5 MPa, the recovery gain from a higher specified injection rate becomes smaller. The cumulative recovery factors of the 20, 40 and 80 t/d cases at the main evaluation time are 23.51%, 23.85% and 23.95%: raising the rate from 20 to 40 t/d adds about 0.34 percentage points, and raising it from 40 to 80 t/d adds only about 0.10 percentage points. The corresponding increments are smaller again at the extended evaluation time (Figure 12b). In this local comparison at fixed conversion and producer pressures, further increases in the specified injection rate bring limited improvement in cumulative recovery.

The conversion timing and the producer pressure act in the same direction as in the single-factor analysis. Raising the conversion pressure from 3 MPa to 4 MPa lowers the cumulative recovery factor at the main evaluation time from 23.85% for R10 to 23.75% for V3, whereas lowering the producer pressure from 7.5 MPa to 6 MPa raises it from 23.85% to 26.88% for V4, which again shows the dominant role of the producer pressure.

The incremental CH_4 per unit of injected CO_2 shows the difference between injection input and recovery gain more directly (Table 9). At the main evaluation time V1, V2 and V3 give 4.43, 4.51 and 4.35 kmol/t, and at the extended evaluation time 4.37, 4.57 and 4.33 kmol/t. A case with a higher injection rate can have a larger absolute incremental recovery while its incremental production per unit of injected CO_2 is not necessarily higher; this indicator is used together with the cumulative recovery factor and the net CO_2 inventory increase when the cases are compared.

The supplementary runs show that the deviation in the additive main-effect prediction differs between combinations (Figure 12a). With the incremental recovery as the response, V1, selected at the main evaluation time, gives a simulated value of 3.59 percentage points against a predicted 3.62 percentage points, whereas V2, selected at the extended evaluation time, gives a simulated 3.51 percentage points against a predicted 3.97 percentage points, a difference of about 0.46 percentage points. The additive main-effect model therefore does not describe all combinations completely, and candidate cases still have to be checked by direct simulation. V1 and V2 were screened for incremental recovery and are not the cases with the highest cumulative recovery factor or the highest CO_2 storage.



(**a**) (**b**)

Figure 12. Incremental recovery of the supplementary cases, in percentage points: (**a**) additive main-effect prediction against simulation for V1 (main evaluation time) and V2 (extended evaluation time); (**b**) incremental recovery versus specified injection rate at a conversion pressure of 3 MPa and a producer pressure of 7.5 MPa.

Table 9. Simulation-derived performance indicators for the supplementary cases at the two evaluation times.

Evaluation Time	Case	CH_4 Recovery Factor/%	Recovery Gain Over Depletion (pp)	CO_2 Storage (10^4 t)	Cumulative CO_2 Injected (10^4 t)	Incremental CH_4 per Injected CO_2 (kmol/t)
t = 22 years	V1	23.95	**3.59**	20.24	20.44	4.43
t = 22 years	V2	23.51	3.15	17.44	17.60	**4.51**
t = 22 years	V3	23.75	3.39	19.47	19.65	4.35
t = 22 years	V4	**26.88**	3.26	**21.39**	21.64	3.80
t = 27 years	V1	24.12	**3.76**	21.49	21.70	4.37
t = 27 years	V2	23.87	3.51	19.19	19.35	**4.57**
t = 27 years	V3	23.97	3.61	20.80	21.00	4.33
t = 27 years	V4	**26.95**	3.32	**22.86**	23.11	3.62

Note: Recovery gain and additional CH_4 production are calculated relative to the continued-depletion case at the same producer BHP and evaluation time (Table 8); pp denotes percentage points. Incremental CH_4 per injected CO_2 equals this additional CH_4 production (kmol) divided by cumulative CO_2 injection (t). Bold values identify maxima among V1–V4 at each evaluation time for the highlighted metrics.

3.6. Selection of the Injection–Production Strategy

Among the orthogonal and supplementary cases computed here, gas recovery and CO_2 storage point to different combinations (Table 10). Case R5 = (20 t/d, 3 MPa, 3 MPa) gives the highest cumulative CH_4 recovery factor, 32.24% and 32.42% at the two evaluation times, and suits a gas-recovery objective. Case R25 = (100 t/d, 3 MPa, 4 MPa) gives the highest CO_2 storage but a lower recovery factor than R5 and R9. The CO_2 mole fraction distributions of R5 and R25 at 22 and 27 years of injection are shown in Figure 13. The two cases differ in both specified injection rate and producer pressure, which illustrates how different combinations serve the recovery and storage objectives. Both convert the central well when its bottom-hole pressure falls to 3 MPa and operate the producers at 3–4 MPa, so a low producer pressure and a late conversion are common to both.

With the injector bottom-hole pressure limited to 45 MPa, R9 = (40t/d, 4 MPa, 3 MPa) was selected as the preferred engineering compromise among the evaluated cases. The selection criterion was to retain a cumulative CH_4 recovery factor close to the highest simulated value while achieving a net CO_2 inventory increase close to the highest simulated value. The trade-off was assessed by direct comparison with the recovery-oriented case R5 and the higher-storage cases R17 and R25, without assigning numerical weights to the two indicators.

At t = 22 years, R9 gives a cumulative CH_4 recovery factor of 31.86% and a net CO_2 inventory increase of 24.12 × 10^4 t. Compared with R5, selecting R9 reduces recovery by 0.38 percentage points while increasing the net CO_2 inventory by 4.33 × 10^4 t, or 21.88%. Compared with R17, R9 achieves a 0.59 percentage-point increase in cumulative CH_4 recovery, while its net CO_2 inventory increase decreases by only 0.03 × 10^4 t (approximately 0.12%) at t = 22 years. Compared with R25, R9 provides 1.53 percentage points higher recovery with a reduction of 0.19 × 10^4 t, or 0.78%, in the net CO_2 inventory increase. At t = 27 years, R9 and R25 have the same net CO_2 inventory increase at the reported precision, approximately 25.63 × 10^4 t, while R9 retains a recovery advantage of

1.54 percentage points. These comparisons support R9 as a preferred compromise for the investigated well group, parameter combinations and evaluation times. The selections for the different objectives are summarized in Table 11.

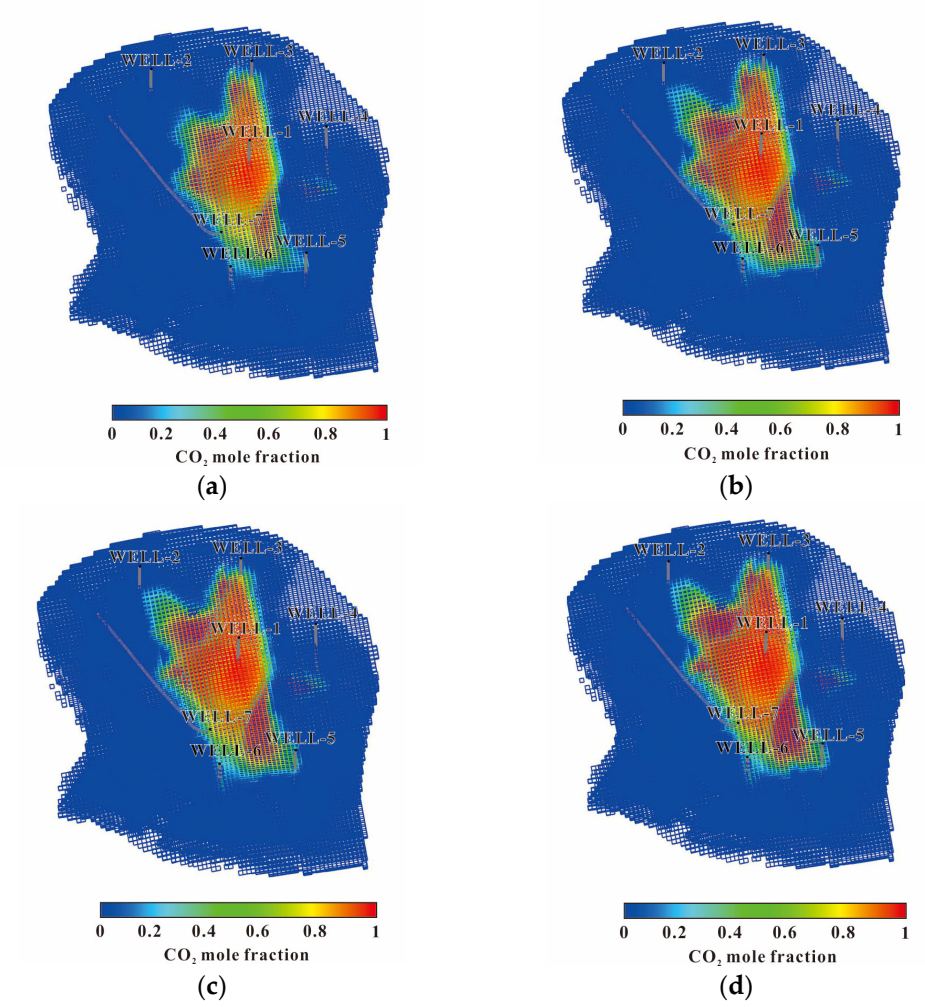


Figure 13. Gas-phase CO_2 mole fraction distribution of cases R5 and R25 at different injection times: (**a**) R5 after 22 years of injection; (**b**) R5 after 27 years; (**c**) R25 after 22 years; (**d**) R25 after 27 years.

Table 10. Representative cases for gas recovery and CO_2 storage in the multifactor design.

Evaluation Time	Case	A/(t/d)	B/MPa	C/MPa	CH_4 Recovery Factor/%	$\Delta M_{CO2}/(10^4$ t)
t = 22 years	R5	20	3	3	32.24	19.79
t = 22 years	R9	40	4	3	31.86	24.12
t = 22 years	R17	80	8	3	31.27	24.15
t = 22 years	R25	100	3	4	30.33	24.31
t = 27 years	R5	20	3	3	32.42	22.42
t = 27 years	R9	40	4	3	31.87	25.63
t = 27 years	R25	100	3	4	30.33	25.63

Table 11. Injection–production strategy for different development objectives.

Case	Objective	Injection Rate/(t/d)	Conversion Pressure/MPa	Producer BHP/MPa	Basis for Selection
R5	Gas recovery	20	3	3	Highest cumulative recovery factor
R9	Recovery and storage	40	4	3	High recovery, storage close to R25

R25	CO_2 storage	100	3	4	Highest storage; matches R9 at t = 27 years

4. Conclusions

A numerical model of an actual well group in the eastern Sulige gas field was built with CO_2 dissolution, adsorption, diffusion, threshold pressure gradient and stress sensitivity. The effect of these mechanism properties on CO_2 flooding was compared and the injection–production strategy was selected. The main conclusions are as follows.

(1) Converting the central well to CO_2 injection after 10 years of depletion raises the cumulative CH_4 recovery factor at 22 years after conversion from 25.88% to 29.00%, and the gain becomes visible about ten months after conversion. The net CO_2 inventory increase over the evaluation period follows the actual injected volume; this indicator describes the inventory change relative to the specified reference state and is not equivalent to a long-term secure storage capacity.

(2) Over the ranges examined, the threshold pressure gradient and the diffusion coefficient give the largest response in stage recovery, changing the incremental recovery within 22 years after conversion by 4.07 and 3.66 percentage points, while dissolution and adsorption change it by less than 0.5 percentage points. A change in any property affects both the reservoir state reached before conversion and the actual injection and production after conversion. Stress sensitivity ranks the cases differently for stage and full-cycle recovery, so it must be assessed over both the depletion and the flooding stages.

(3) Injectivity is limited by the injection pressure constraint. Cases with a high specified injection rate switch to pressure control earlier, and their recovery advantage does not persist to the extended evaluation time. Within 43–45 MPa, a further increase in injection pressure brings little additional recovery.

(4) For this well group and the factor levels examined, the producer bottom-hole pressure produces the largest response in cumulative recovery: lowering it from 7.5 MPa to 3 MPa raises the recovery factor by about 8.4 percentage points. The conversion pressure of the central well ranks second, with a later conversion adding 1.02 percentage points, and the main effect of the specified injection rate is weak.

(5) With the injector bottom-hole pressure limited to 45 MPa and within the combinations computed, R5 (20 t/d, 3 MPa, 3 MPa) gives the highest cumulative recovery factor of 32.24% when gas recovery is the objective. When recovery and CO_2 storage are considered together, R9 (40 t/d, 4 MPa, 3 MPa) is the compromise, giving a recovery factor of 31.86% and a CO_2 storage of 24.12×10^4 t at the main evaluation time, that is, about 22% more storage at the cost of less than 0.4 percentage points of recovery.

The main scientific contribution of this study is the integrated evaluation of multiple transport and flow mechanisms and injection–production strategies within a heterogeneous tight gas well-group model. By distinguishing injection-stage recovery from cumulative recovery and considering actual CO_2 injection under pressure constraints, the study provides a consistent basis for assessing the trade-off between gas recovery and CO_2 storage. From an engineering perspective, the results highlight the importance of coordinating producer bottom-hole pressure, well-conversion timing, and injection rate rather than optimizing individual parameters independently. Nevertheless, the proposed optimization is limited to the investigated parameter combinations and does not incorporate economic objectives or a formal weighted multi-objective optimization framework. In addition, the model was not validated against historical production and reservoir pressure data, and geological uncertainty was not systematically quantified. The model also adopted several simplifying assumptions, including closed reservoir boundaries without external aquifer support, a common representative gas–water relative permeability curve, a constant effective diffusion coefficient, and independent-component adsorption relationships. Furthermore, formal grid-refinement analysis and long-term

post-injection CO_2 containment assessment were not performed. Therefore, the selected operating strategy should be regarded as a simulation-based candidate requiring further field validation and uncertainty assessment before practical implementation.

Author Contributions: Conceptualization, P.L. and Z.Y.; Methodology, P.L. and X.Z.; Software, J.L.; Validation, X.Z. and J.L.; Formal analysis, P.L. and L.L.; Investigation, L.L.; Resources, X.L. and L.L.; Data curation, J.L.; Writing—original draft, P.L.; Writing—review and editing, X.Z., X.L. and Z.Y.; Visualization, P.L.; Supervision, X.L. and Z.Y.; Project administration, Z.Y.; Funding acquisition, L.L. All authors have read and agreed to the published version of the manuscript.

Funding: This research was funded by the Science and Technology Project of PetroChina Company Limited, "Research on Energy Supplementation to Enhance Recovery in Tight Gas Reservoirs" (No. 2023ZZ25YJ05).

Data Availability Statement: The original contributions presented in this study are included in the article. Further inquiries can be directed to the corresponding author.

Acknowledgments: We would like to thank Tiezhu Tang for providing valuable technical assistance in software execution and data collection during this study.

Conflicts of Interest: Author Pengcheng Liu, Lili Liu and Jun Liu was employed by the company PetroChina Changqing Oilfield Company. The remaining authors declare that the research was conducted in the absence of any commercial or financial relationships that could be construed as a potential conflict of interest.

References

1. Dai, J.; Ni, Y.; Wu, X. Tight Gas in China and Its Significance in Exploration and Exploitation. *Pet. Explor. Dev.* **2012**, *39*, 277–284. https://doi.org/10.1016/S1876-3804(12)60043-3.
2. Zou, C.; Zhu, R.; Liu, K.; Su, L.; Bai, B.; Zhang, X.; Yuan, X.; Wang, J. Tight Gas Sandstone Reservoirs in China: Characteristics and Recognition Criteria. *J. Pet. Sci. Eng.* **2012**, *88–89*, 82–91. https://doi.org/10.1016/j.petrol.2012.02.001.
3. Yang, H.; Fu, J.; Liu, X.; Meng, P. Accumulation Conditions and Exploration and Development of Tight Gas in the Upper Paleozoic of the Ordos Basin. *Pet. Explor. Dev.* **2012**, *39*, 315–324. https://doi.org/10.1016/S1876-3804(12)60047-0.
4. He, D.; Jia, A.; Ji, G.; Wei, Y.; Tang, H. Well Type and Pattern Optimization Technology for Large Scale Tight Sand Gas, Sulige Gas Field, NW China. *Pet. Explor. Dev.* **2013**, *40*, 84–95. https://doi.org/10.1016/S1876-3804(13)60008-7.
5. Oldenburg, C.M.; Pruess, K.; Benson, S.M. Process Modeling of CO_2 Injection into Natural Gas Reservoirs for Carbon Sequestration and Enhanced Gas Recovery. *Energy Fuels* **2001**, *15*, 293–298. https://doi.org/10.1021/ef000247h.
6. Oldenburg, C.M.; Stevens, S.H.; Benson, S.M. Economic Feasibility of Carbon Sequestration with Enhanced Gas Recovery (CSEGR). *Energy* **2004**, *29*, 1413–1422. https://doi.org/10.1016/j.energy.2004.03.075.
7. Liu, S.-Y.; Ren, B.; Li, H.-Y.; Yang, Y.-Z.; Wang, Z.-Q.; Wang, B.; Xu, J.-C.; Agarwal, R. CO_2 Storage with Enhanced Gas Recovery (CSEGR): A Review of Experimental and Numerical Studies. *Pet. Sci.* **2022**, *19*, 594–607. https://doi.org/10.1016/j.petsci.2021.12.009.
8. Wei, N.; Jiao, Z.; Ellett, K.; Ku, A.Y.; Liu, S.; Middleton, R.; Li, X. Decarbonizing the Coal-Fired Power Sector in China via Carbon Capture, Geological Utilization, and Storage Technology. *Environ. Sci. Technol.* **2021**, *55*, 13164–13173. https://doi.org/10.1021/acs.est.1c01144.
9. Sim, S.S.K.; Turta, A.T.; Singhal, A.K.; Hawkins, B.F. *Enhanced Gas Recovery: Factors Affecting Gas-Gas Displacement Efficiency*; OnePetro: Richardson, TX, USA, 2008.
10. Sidiq, H.; Amin, R.; der Steen, E.V.; Kennaird, T. Super Critical CO_2–Methane Relative Permeability Investigation. *J. Pet. Sci. Eng.* **2011**, *78*, 654–663. https://doi.org/10.1016/j.petrol.2011.08.018.
11. Hughes, T.J.; Honari, A.; Graham, B.F.; Chauhan, A.S.; Johns, M.L.; May, E.F. CO_2 Sequestration for Enhanced Gas Recovery: New Measurements of Supercritical CO_2–CH_4 Dispersion in Porous Media and a Review of Recent Research. *Int. J. Greenh. Gas Control* **2012**, *9*, 457–468. https://doi.org/10.1016/j.ijggc.2012.05.011.

12. Honari, A.; Hughes, T.J.; Fridjonsson, E.O.; Johns, M.L.; May, E.F. Dispersion of Supercritical CO_2 and CH_4 in Consolidated Porous Media for Enhanced Gas Recovery Simulations. *Int. J. Greenh. Gas Control* **2013**, *19*, 234–242. https://doi.org/10.1016/j.ijggc.2013.08.016.
13. Patel, M.J.; May, E.F.; Johns, M.L. High-Fidelity Reservoir Simulations of Enhanced Gas Recovery with Supercritical CO_2. *Energy* **2016**, *111*, 548–559. https://doi.org/10.1016/j.energy.2016.04.120.
14. Kühn, M.; Tesmer, M.; Pilz, P.; Meyer, R.; Reinicke, K.; Förster, A.; Kolditz, O.; Schäfer, D.; CLEAN Partners CLEAN: Project Overview on CO_2 Large-Scale Enhanced Gas Recovery in the Altmark Natural Gas Field (Germany). *Environ. Earth Sci.* **2012**, *67*, 311–321. https://doi.org/10.1007/s12665-012-1714-z.
15. Hamza, A.; Hussein, I.A.; Al-Marri, M.J.; Mahmoud, M.; Shawabkeh, R.; Aparicio, S. CO_2 Enhanced Gas Recovery and Sequestration in Depleted Gas Reservoirs: A Review. *J. Pet. Sci. Eng.* **2021**, *196*, 107685. https://doi.org/10.1016/j.petrol.2020.107685.
16. Hussen, C.; Amin, R.; Madden, G.; Evans, B. Reservoir Simulation for Enhanced Gas Recovery: An Economic Evaluation. *J. Nat. Gas Sci. Eng.* **2012**, *5*, 42–50. https://doi.org/10.1016/j.jngse.2012.01.010.
17. Jia, Y.; Shi, Y.; Pan, W.; Huang, L.; Yan, J.; Zhao, Q. The Feasibility Appraisal for CO_2 Enhanced Gas Recovery of Tight Gas Reservoir: Experimental Investigation and Numerical Model. *Energies* **2019**, *12*, 2225. https://doi.org/10.3390/en12112225.
18. Zhao, E.-M.; Jin, Z.-J.; Li, G.-S.; Zhang, K.-Q.; Zeng, Y. Feasibility of CO_2 Storage and Enhanced Gas Recovery in Depleted Tight Sandstone Gas Reservoirs within Multi-Stage Fracturing Horizontal Wells. *Pet. Sci.* **2024**, *21*, 4189–4203. https://doi.org/10.1016/j.petsci.2024.08.014.
19. Zhao, E.; Jin, Z.; Li, G.; Zhang, K.; Zeng, Y. Numerical Simulation of CO_2 Storage with Enhanced Gas Recovery in Depleted Tight Sandstone Gas Reservoirs. *Fuel* **2024**, *371*, 131948. https://doi.org/10.1016/j.fuel.2024.131948.
20. Zhao, E.; Jin, Z.; Li, G.; Hou, J.; Zeng, Y Potential Assessment and Production Performance Analysis of CO_2 Storage with Enhanced Gas Recovery from Tight Gas Reservoirs. *Phys. Fluids* **2025**, *37*, 063103. https://doi.org/10.1063/5.0273831.
21. Liu, Z.; Niu, J.; Guo, Y.; Jia, Y.; Cui, M. Mechanisms of CO_2 Enhanced Gas Recovery in Tight-Sand Gas Reservoirs. *Energy Geosci.* **2025**, *6*, 100393. https://doi.org/10.1016/j.engeos.2025.100393.
22. Hu, J.; Yang, S.; Yang, K.; Deng, H.; Wang, M.; Li, J.; Gao, X. Enhanced Gas Recovery Coupled with CO_2 Sequestration in Tight Sandstone Reservoirs with Different Pore-Throat Structures. *Energy Fuels* **2024**, *38*, 12005–12023. https://doi.org/10.1021/acs.energyfuels.4c01971.
23. Ding, J.; Yan, C.; He, Y.; Wang, C. Supercritical CO_2 Sequestration and Enhanced Gas Recovery in Tight Gas Reservoirs: Feasibility and Factors That Influence Efficiency. *Int. J. Greenh. Gas Control* **2021**, *105*, 103234. https://doi.org/10.1016/j.ijggc.2020.103234.
24. Yan, H.; Cheng, G.; Guo, J.; Wang, R.; Ning, B.; Wang, X.; Yuan, H.; Liu, H. Study on CO_2 Induced Gas Channeling in Tight Gas Reservoirs and Optimization of Injection Production Parameters. *Energies* **2025**, *18*, 5584. https://doi.org/10.3390/en18215584.
25. Liu, Z.; Zhang, H.; Zhao, R.; He, L.; Zhang, B.; Yuan, Y.; Zhao, K. CO_2 Injection for Enhanced Gas Recovery in Tight Gas Reservoirs of the Central Shenfu Area. *Energies* **2026**, *19*, 801. https://doi.org/10.3390/en19030801.
26. Duan, Z.; Sun, R. An Improved Model Calculating CO_2 Solubility in Pure Water and Aqueous NaCl Solutions from 273 to 533 K and from 0 to 2000 Bar. *Chem. Geol.* **2003**, *193*, 257–271. https://doi.org/10.1016/S0009-2541(02)00263-2.
27. Spycher, N.; Pruess, K.; Ennis-King, J. CO_2-H_2O Mixtures in the Geological Sequestration of CO_2. I. Assessment and Calculation of Mutual Solubilities from 12 to 100 °C and up to 600 Bar. *Geochim. Cosmochim. Acta* **2003**, *67*, 3015–3031. https://doi.org/10.1016/S0016-7037(03)00273-4.
28. Ding, J.; Yan, C.; Wang, G.; He, Y.; Zhao, R. Competitive Adsorption between CO_2 and CH_4 in Tight Sandstone and Its Influence on CO_2-Injection Enhanced Gas Recovery (EGR). *Int. J. Greenh. Gas Control* **2022**, *113*, 103530. https://doi.org/10.1016/j.ijggc.2021.103530.
29. Prada, A.; Civan, F. Modification of Darcy's Law for the Threshold Pressure Gradient. *J. Pet. Sci. Eng.* **1999**, *22*, 237–240. https://doi.org/10.1016/S0920-4105(98)00083-7.
30. Zeng, B.; Cheng, L.; Li, C. Low Velocity Non-Linear Flow in Ultra-Low Permeability Reservoir. *J. Pet. Sci. Eng.* **2011**, *80*, 1–6. https://doi.org/10.1016/j.petrol.2011.10.006.
31. Ding, J.; Yang, S.; Nie, X.; Wang, Z. Dynamic Threshold Pressure Gradient in Tight Gas Reservoir. *J. Nat. Gas Sci. Eng.* **2014**, *20*, 155–160. https://doi.org/10.1016/j.jngse.2014.06.019.
32. Zhong, X.; Zhu, Y.; Liu, L.; Yang, H.; Li, Y.; Xie, Y.; Liu, L. The Characteristics and Influencing Factors of Permeability Stress Sensitivity of Tight Sandstone Reservoirs. *J. Pet. Sci. Eng.* **2020**, *191*, 107221. https://doi.org/10.1016/j.petrol.2020.107221.

33. Liu, P.; Jia, C. Dynamic Mohr-Coulomb Evaluation of Natural Fracture Stability in Deep Shale under Hydraulic Fracturing Induced Stress Superposition. *Adv. Geo-Energy Res.* **2026**, *20*, 213–226. https://doi.org/10.46690/ager.2026.06.04.
34. Cao, N.; Lei, G. Stress Sensitivity of Tight Reservoirs during Pressure Loading and Unloading Process. *Pet. Explor. Dev.* **2019**, *46*, 138–144. https://doi.org/10.1016/S1876-3804(19)30013-8.
35. Yang, Z.; Liao, X.; Liu, P.; Liu, P.; AlAhmad, H.A.; Jia, C. Full-Lifecycle Numerical Simulation of CO_2 Storage with Enhanced Gas Recovery in Stress-Sensitive Tight Gas Reservoirs. *Fuel* **2027**, *427*, 140086. https://doi.org/10.1016/j.fuel.2026.140086.
36. Liu, L.; Li, J.; Liu, P.; Yang, Z.; Fu, B.; Liao, X. Study on Main Controlling Factors of CO_2 Enhanced Gas Recovery and Geological Storage in Tight Gas Reservoirs. *Processes* **2025**, *13*, 3097. https://doi.org/10.3390/pr13103097.
37. Ding, S.; Liu, Q.; Li, P.; Wang, L.; Li, Y.; Zhang, M.; Xu, C.; Ma, J. An Efficient Hybrid Methodology for Optimization of CO_2 Huff-n-Puff EOR and Sequestration in Tight Oil Reservoirs. *Int. J. Greenh. Gas Control* **2024**, *132*, 104062. https://doi.org/10.1016/j.ijggc.2024.104062.
38. Peng, D.-Y.; Robinson, D.B. A New Two-Constant Equation of State. *J. Ind. Eng. Chem. Fundam.* **1976**, *15*, 59–64. https://doi.org/10.1021/i160057a011.
39. Lohrenz, J.; Bray, B.G.; Clark, C.R. Calculating Viscosities of Reservoir Fluids From Their Compositions. *J. Pet. Technol.* **1964**, *16*, 1171–1176. https://doi.org/10.2118/915-PA.
40. Coats, K.H. An Equation of State Compositional Model. *Soc. Pet. Eng. J.* **1980**, *20*, 363–376. https://doi.org/10.2118/8284-PA.
41. Davies, J.P.; Davies, D.K. *Stress-Dependent Permeability: Characterization and Modeling*; OnePetro: Richardson, TX, USA, 1999.
42. Langmuir, I. The adsorption of gases on plane surfaces of glass, mica and platinum. *J. Am. Chem. Soc.* **1918**, *40*, 1361–1403. https://doi.org/10.1021/ja02242a004.
43. Li, Y.-K.; Nghiem, L.X. Phase Equilibria of Oil, Gas and Water/Brine Mixtures from a Cubic Equation of State and Henry's Law. *Can. J. Chem. Eng.* **1986**, *64*, 486–496. https://doi.org/10.1002/cjce.5450640319.

Disclaimer/Publisher's Note: The statements, opinions and data contained in all publications are solely those of the individual author(s) and contributor(s) and not of MDPI and/or the editor(s). MDPI and/or the editor(s) disclaim responsibility for any injury to people or property resulting from any ideas, methods, instructions or products referred to in the content.